
High-Performance Nonvolatile Spin FETs from 2D Metallic Ferromagnetic and Ferroelectric Multiferroic Heterostructure

B. Liu¹, X. Zhang^{2,‡}, W. Hou¹, H. Feng¹, Z. Dai^{1,‡}, and Zhi-Xin Guo^{1,†}

¹*State Key Laboratory for Mechanical Behavior of Materials, Xi'an Jiaotong University, Xi'an, Shaanxi, 710049, China.*

²*Shaanxi Key Laboratory of Surface Engineering and Remanufacturing College of Mechanical and Materials Engineering Xi'an University, Xi'an 710065, China.*

†zhangxian1@outlook.com

‡sensdai@mail.xjtu.edu.cn

*zxguo08@xjtu.edu.cn

Abstract: All-electric-controlled nonvolatile spin field-effect transistors (SFETs) based on two-dimensional (2D) multiferroic van der Waals (vdW) heterostructures hold great promise for advanced spintronics applications. However, their performance is hindered by the limited availability of 2D magnetic materials that can switch effectively between metallic and semiconducting states with sizable bandgaps controlled by ferroelectric polarization. Most studies have focused on materials that are naturally semiconducting, achieving a metallic state by modifying the ferroelectric polarization. In this work, we introduce an innovative approach that uses interface effects to convert inherently metallic 2D magnetic materials into half-metals and induce half-semiconducting behavior through changes in ferroelectric polarization. Density functional theory (DFT) calculations on the CrPS₃/Sc₂CO₂ heterostructure demonstrate that the ferroelectric polarization of Sc₂CO₂ monolayers can adjust the electronic structure of CrPS₃, enabling a switch from half-metallic to half-semiconducting states. Building on these insights, we designed a nonvolatile SFET and analyzed its transport properties using the nonequilibrium Green's function (NEGF) method combined with DFT. Our results show that reversing the ferroelectric polarization achieves an on/off current ratio exceeding 5×10^6 %, and the heterostructure generates nearly 100 % spin-polarized current with a current density of up to 6500 $\mu\text{A}/\mu\text{m}$ at bias voltage below 0.2 V. These findings highlight a promising pathway for developing high-performance SFETs that surpass existing 2D heterojunction materials.

1. Introduction:

Spintronics is believed to be a strong candidate of the future technology in the post-Si era. Practical applications of spintronics rely on key processes such as spin injection, detection, manipulation, and storage [1,2]. All-electric-controlled spin field effect transistor (SFET) is a fundamental spin-based device for the spin operation, which has attracted considerable research attention [3-6]. Advancing spintronics requires the development of SFETs that combine low power consumption, high performance, and efficient pure spin current switching.

A promising candidate for efficient SFETs is two-dimensional (2D) ferromagnetic (FM) half-metallic materials, which can generate 100% spin-polarized current by exhibiting metallic behavior in one spin channel and semiconducting or insulating behavior in the other. However, intrinsically half-metallic 2D materials are rare [7-10]. Although external modulation techniques such as electric fields and strain can induce half-metallicity [11], these approaches lack nonvolatility, limiting their practical applications. Recent progress in van der Waals (vdW) multiferroic heterojunctions, combining 2D ferroelectrics with 2D FM materials, offers a promising alternative. These multiferroic heterojunctions enable fully electric-controlled gating effects, paving the way for low-power and nonvolatile SFETs [12-21].

In the multiferroic heterojunctions, 2D ferroelectrics not only provide nonvolatility but also open new possibilities for spintronic devices. To date, research on 2D multiferroic heterojunctions has primarily focused on materials with intrinsic half-semiconducting properties, such as H-FeCl₂ [15], VSi₂N₄ [14,19], GdF₂ [21], and MnI₃ [20]. In these studies, metallic states are achieved by altering the ferroelectric polarization of the ferroelectric material. However, the performance of SFETs is limited by the scarcity of 2D semiconducting magnetic materials that can effectively switch between metallic and semiconducting states with sizable bandgaps controlled by ferroelectric polarization.

This study proposes a novel method that leverages interface effects to transform intrinsically metallic 2D magnetic materials into half-metals and induce half-semiconductor characteristics through changes in the ferroelectric polarization of 2D ferroelectric materials. As a proof of concept, we selected the metallic 2D magnetic material CrPS₃ and the 2D ferroelectric material Sc₂CO₂ to construct a vdW multiferroic heterojunction for use as the channel material in SFETs. First-principles calculations reveal that the monolayer Sc₂CO₂ effectively modifies the electronic structure of CrPS₃,

enabling a transition from half-metallic to semiconducting states. The corresponding SFET demonstrates exceptional performance. Reversing the ferroelectric polarization of Sc_2CO_2 achieves an extraordinarily high *on/off* current ratio exceeding 5×10^6 % under finite bias. Moreover, the heterostructure generates nearly 100 % spin-polarized current with a current density of up to $6500 \mu\text{A}/\mu\text{m}$ at voltages below 0.2 V.

Results and discussion:

The heterostructure consists of a monolayer CrPS_3 and a monolayer Sc_2CO_2 . As shown in Fig. 1(a), freestanding monolayer CrPS_3 is a magnetic material with a triangular lattice, where Cr atoms reside within octahedra formed by S atoms, and its optimized lattice constant is 5.90 \AA , consistent with previous studies [22-24]. Although the freestanding monolayer CrPS_3 was reported to hold an antiferromagnetic (AFM) ground state [24,25], we find it has a FM ground state (180 meV more stable than the AFM state) in the heterostructure, as discussed below. As shown in Fig. 1(b), the FM phase of monolayer CrPS_3 exhibits excellent metallic characteristic, with a mix of spin-up and spin-down electronic bands around the Fermi energy (E_F). On the other hand, monolayer Sc_2CO_2 (Fig. 1(c)) also possesses a triangular lattice and is a ferroelectric material (out-of-plane polarization of $1.60 \mu\text{C}/\text{cm}^2$) with an optimized lattice constant of 3.43 \AA , in agreement with prior works [26,27]. As depicted in Fig. 1(d), its band structure displays a large bandgap of approximately 1.84 eV between the VBM and CBM, consistent with previous studies.

In the heterostructure, a 1×1 unit cell of CrPS_3 is commensurate with $\sqrt{3} \times \sqrt{3}$ unit cell of Sc_2CO_2 , resulting a lattice mismatch less than 5 %. As illustrated in Fig. S1, we explored four typical stacking configurations, with the corresponding energy calculations presented in Table S1. The lowest energy structure is shown in Fig. 2. The structural distortion at the CrPS_3 - Sc_2CO_2 interface, induced by the presence of Sc_2CO_2 , causes a downward shift of phosphorus atoms, which significantly alters the electronic structure. Notably, the ground state of CrPS_3 exhibits an AFM state [24,25], warranting an investigation into the magnetic ground state of the heterostructure. We calculated four magnetic states, as depicted in Fig. S2. The results indicate that regardless of the polarization direction, the CrPS_3 always has a FM ground state in the heterostructure, with the total energy being more than 180 meV lower than that of any other magnetic state (see Table S2).

It is noted that the interlayer surface atoms of the heterostructure are oxygen for Sc_2CO_2 and phosphorus atoms for CrPS_3 , with atomic radii of 0.66 \AA and 1.05 \AA ,

respectively. Given that the interlayer distances in the $P\uparrow$ and $P\downarrow$ polarization states are 2.58 Å and 2.63 Å, which are substantially larger than the sum of the oxygen and phosphorus atomic radii, a vdW interaction exists between CrPS_3 and Sc_2CO_2 . To ensure energetic stability, we further calculated the binding energy (E_b) between CrPS_3 and Sc_2CO_2 , defined as $E_b=(E_{\text{tot}}-E_{\text{CrPS}_3}-E_{\text{Sc}_2\text{CO}_2})/S$, where E_{tot} , E_{CrPS_3} , and $E_{\text{Sc}_2\text{CO}_2}$ represent the total energy of the heterojunction, the energy of monolayer CrPS_3 , and the energy of monolayer Sc_2CO_2 , respectively, and S denotes the interface area of the simulation cell. In the $P\uparrow$ and $P\downarrow$ polarization states, E_b values are $-26.18 \text{ meV}/\text{Å}^2$ and $-18.43 \text{ meV}/\text{Å}^2$, respectively, confirming the energetic stability of the heterostructure.

We now examine the influence of Sc_2CO_2 on the electronic structure of CrPS_3 which primarily governs the spin current. Despite the persistence of weak vdW interaction, we find that it still results in a sizable downward displacement of phosphorus atoms at the interface, significantly affecting the band structure of CrPS_3 . Compared to the band structure of freestanding CrPS_3 [Fig. 1(b)], in the $P\uparrow$ polarization state, the spin-down electronic band of CrPS_3 exhibits a substantial bandgap of 1.02 eV. Meanwhile, the spin-up electronic band intersects the Fermi level, transforming CrPS_3 into a half-metal with 100% spin polarization, as shown in Fig. 2(b). This confirms that the conversion of regular metallic CrPS_3 to a half-metal via interface effects has been successfully achieved. Furthermore, there are no electronic bands crossing the Fermi level, indicating minimal contribution of Sc_2CO_2 to the electronic transport in the heterostructure.

When the polarization of Sc_2CO_2 shifts to the $P\downarrow$ state, the phosphorus atoms at the interface undergo a significant downward displacement due to the vdW interaction from Sc_2CO_2 . Both the conduction band minimum (CBM) and the valence band maximum (VBM) in the spin-up and spin-down states are primarily contributed by CrPS_3 , illustrating a type-I band alignment. This result demonstrates that the $P\downarrow$ polarization of Sc_2CO_2 transforms CrPS_3 into a semiconductor with a large bandgap. Compared to the $P\uparrow$ state where the CrPS_3 is a half-metal (zero/1.02 eV band gap for spin-up/spin-down electrons), in the $P\downarrow$ state the CrPS_3 has a spin-up bandgap of 0.77 eV and a spin-down bandgap of 1.18 eV. This suggests that the electronic properties of CrPS_3 are heavily influenced by the out-of-plane polarization of Sc_2CO_2 . It is noticed that in energy range around CBM, the electronic states are purely from spin-up electrons, making CrPS_3 a half-semiconductor characteristic. The above results manifest that reversing polarization of Sc_2CO_2 induces a half-metal to half-semiconductor transition in CrPS_3 with 100% spin-up polarization, which may have good performance in the

SFETs.

To further investigate the effects of Sc_2CO_2 polarization on electronic band structures of CrPS_3 , we calculated the potential difference and charge transfer density of the heterostructure. Figures 3(a) and 3(c) illustrate the averaged potential differences for the heterostructure with spontaneous vertical polarization oriented upwards and downwards, respectively. This vertical polarization generates a potential difference, $\Delta\phi$, between the upper and lower surfaces of the heterostructure. Reversal of the Sc_2CO_2 polarization direction changes the value of $\Delta\phi$ from 1.17 eV in the $P\uparrow$ state to 1.92 eV in the $P\downarrow$ state. The difference in $\Delta\phi$ indicates that once the electric field used to switch the polarization of Sc_2CO_2 is removed, the Sc_2CO_2 monolayer can maintain its polarization state, rendering the heterostructure nonvolatile. Significantly, the interface effects induce structural changes in CrPS_3 , leading to pronounced ferroelectric polarization. The charge transfer density difference ($\Delta\rho$) for the heterostructure is described by the formula $\Delta\rho = \rho_{\text{CrPS}_3/\text{Sc}_2\text{CO}_2} - \rho_{\text{CrPS}_3} - \rho_{\text{Sc}_2\text{CO}_2}$, where $\rho_{\text{CrPS}_3/\text{Sc}_2\text{CO}_2}$, ρ_{CrPS_3} , and $\rho_{\text{Sc}_2\text{CO}_2}$ represent the charge densities of the $\text{CrPS}_3/\text{Sc}_2\text{CO}_2$ heterostructure, the monolayer CrPS_3 , and the monolayer Sc_2CO_2 , respectively (Figs. 3(b) and 3(d)). Integration of $\Delta\rho$ along the out-of-plane (z) direction reveals that in the $P\uparrow$ state, electrons transfer from the surface of Sc_2CO_2 to CrPS_3 , with a significant transfer of up to 1.5 electrons. Notably, the significant charge transfer from Sc_2CO_2 to CrPS_3 is mainly attributed to spin-up electrons, and the spin-down electrons primarily transfer to the interface center, as depicted in Fig. S3. On the other hand, when Sc_2CO_2 is polarized to the $P\downarrow$ state, ferroelectric polarization induces minor charge transfer, i.e., the both electrons of Sc_2CO_2 and CrPS_3 transfer to the interface center (with only 0.47 electrons transferred). The polarization direction of Sc_2CO_2 strongly influences the charge transfer process [14], leading to distinct spin-polarized band structures in CrPS_3 (Fig. 2). This behavior is expected to enable distinguished nonvolatile SFET performance.

To verify the above prospection, we further designed a nonvolatile SFET device utilizing the vertically stacked heterostructure, as illustrated in Fig. 4(a). When Sc_2CO_2 is polarized to the $P\uparrow$ state CrPS_3 generates a 100% spin-polarized current due to its half-metal characteristics. In this case, the SFET is in the "on" state. Conversely, when Sc_2CO_2 is polarized to the $P\downarrow$ state, a significant bandgap in the CrPS_3 spin-up electronic band predicts a very small spin-up transmission current in the low bias voltage region, placing the SFET is in the "off" state. Note that the spin-down electronic band always exhibits a sizable bandgap in both $P\uparrow$ and $P\downarrow$ states, contributing to little transmission current. Hence, the heterojunction is expected to display rich nonvolatile

spin transport characteristics with excellent device performance.

To validate these assertions, we calculated the electronic transport properties of the heterojunction SFET. Figures 4(b) and 4(c) depict the transmission spectra of the device under zero bias for Sc₂CO₂ in the P↑ and P↓ polarization states, respectively. In the P↑ state, in the low energy region of [0.05, 0.7] eV, the transmission rate of spin-up electrons is sizable with a maximum reaching 1.3 at 0.1 eV, while spin-down electrons exhibit nearly no transmission. As shown in Fig. 3(b) and Fig. S4, the sizable spin-up electron transmission is entirely contributed by CrPS₃ in such energy region, confirming the nature of 100% spin-polarized current in the SFET. When Sc₂CO₂ is in the P↓ state, the spin-down transmission spectrum remains zero across a substantial energy range of [-0.2, 0.8] eV, while the spin-up transmission spectrum is zero within the range of [-0.2, 0.2] eV. Thus, in the P↓ state, the spin current is fully suppressed within low finite bias. This result demonstrates that devices based on CrPS₃/Sc₂CO₂ possess excellent spin valve performance.

We additionally investigated the electronic transport behavior of the CrPS₃/Sc₂CO₂ device under low bias voltage of [0, 0.5] V. Figure 5(a) illustrates the total transmission current (the sum of spin-up and spin-down currents) and the corresponding "on/off" ratio. When Sc₂CO₂ is in the P↑ state, a large current is observed within the bias range 0-0.5 V. The current peak reaches at 6623 μA/μm appearing at a bias of 0.1 V and gradually decreases to 3400 μA/μm as the bias increases to 0.5 V, presenting a characteristic of negative differential conductance (NDC). To elucidate the underlying mechanism of the NDC, we further analyzed the transmission spectrum of different bias. As shown in Fig. S5, the transmission clearly decreases as the bias voltage increases from 0.1 to 0.5 V, leading to a significant decrease of the transmission current. On the other hand, in the P↓ state the current remains below 0.3 μA/μm within the bias voltage smaller than 0.5 V and decreases to 0.06 μA/μm at 0.5 V, showing extremely low leakage current. This feature results in remarkably large "on/off" ratio, greater than 2×10^6 as shown in Fig. 5(a). Especially, the "on/off" reaches up to 5.4×10^6 when the bias voltage reaches 0.5 V. In Fig. 5(b), we additionally show the ratio between spin-up/spin-down current for both P↑ and P↓ states. It is seen that the ratio also monotonously increases from 10^3 (10^4) to 8×10^5 (6×10^9) with the bias voltage increasing from 0.1 to 0.5 V for the P↑ (P↓) state, verifying that a nearly 100% spin-polarized current is achieved in the SFET device. These results manifest the excellent performance of CrPS₃/Sc₂CO₂ all-electric-controlled nonvolatile SFETs.

Finally, we conducted a comparative analysis of the CrPS₃/Sc₂CO₂ SFET device

with other reported SFETs based on 2D multiferroic heterostructure reported so far. Table 1 summarizes a comparison on the three significant device parameters among our CrPS₃/Sc₂CO₂ SFET and other SFETs, i.e., *on/off* ratio, spin-up/spin-down current ratio and tunneling electroresistance (TER) (define as $TER = \frac{|T_{\uparrow} - T_{\downarrow}|}{\min(T_{\uparrow}, T_{\downarrow})}$) [16]. It is seen that all these parameters are much more superior to other SFETs reported so far [14-16]. Moreover, the “*on/off*” ratio of the CrPS₃/Sc₂CO₂ SFET device is comparable to that of other conventional 2D vdW ferroelectric field-effect transistors (FeFETs), as shown in Table 1, highlighting the great potential of CrPS₃/Sc₂CO₂ for high-performance non-volatile SFET applications.

Summary:

In summary, we discover that metallic 2D magnetic materials can be an ideal candidate in the multiferroic heterostructure for the high-performance nonvolatile SFET devices. By performing first-principles calculations on CrPS₃/Sc₂CO₂ heterostructure, we confirm that the interface effects from ferroelectric Sc₂CO₂ can convert inherently metallic magnetic CrPS₃ into half-metals and further induce half-semiconducting behavior through changes in ferroelectric polarization. Building on these insights, we designed a nonvolatile SFET based on the CrPS₃/Sc₂CO₂ heterostructure. Electronic transport calculations based on the ENGF method, further show that this SFET exhibits exceptional performance under low bias voltage region [0, 0.5] V. Our results show that reversing the ferroelectric polarization achieves an “*on/off*” current ratio in range of 2×10^6 % to 5.5×10^6 %. Moreover, the on-state currents are very large (3400-6500 $\mu\text{A}/\mu\text{m}$), presenting nearly 100% spin polarization where the ratio between spin-up/spin-down current is greater than 10^3 . The performance of CrPS₃/Sc₂CO₂ device significantly exceeds that of other nonvolatile SFET devices, manifesting the great potential applications of multiferroic heterostructure based on 2D metallic magnetic materials in the high-performance, low-power, non-volatile SFET devices.

Method:

The density functional theory (DFT) with the projector-augmented-wave (PAW) method, which is implemented in the Vienna Ab Initio Simulation Package [28-30], are used for Geometric optimization and electronic structures of the heterostructure. The convergence standards of the atomic energy and positions are less than 1×10^{-5} eV per atom and 1×10^{-2} eV/Å, respectively. The cutoff energy of wave function is set to 520 eV. Uniform k meshes of $12 \times 12 \times 1$ and $21 \times 21 \times 1$ within the Γ -centered Monkhorst-Pack scheme [31] are adopted for the structural optimization and the self-consistent calculations, respectively. The exchange-correlation interaction is treated by the generalized gradient approximation (GGA) based on the Perdew-Burke-Ernzerhof (PBE) function [32] for the geometric optimization and electronic structures. The correlation effects for the d electrons of chromium are incorporated using the GGA+U [33] approach with an on-site effective interaction parameter $U = 3.0$ eV [34]. A vacuum layer of more than 15 Å is used, and the interlayer vdW interactions are treated with the DFT-D2 functional [35].

The transport properties are simulated based on the DFT method combined with the nonequilibrium Green's function (NEGF) formalism [36], via the Quantum-ATK package [37]. The K-point of device is set $7 \times 1 \times 93$ in the transport calculations and the density mesh cutoff is set of 85.0 Hartree. The transmission calculations were carried out using the HGH Tier3 of the PBE pseudopotentials distributed in the Quantum-Wise package. The spin-resolved current at a bias voltage V_b can be calculated as

$$I_\sigma(V_b) = \frac{e}{h} \int_{-\infty}^{+\infty} dE [f(E, \mu_L) - f(E, \mu_R)] T_\sigma(E, V_b). \quad (1)$$

Here the $f(E, \mu_L)$ and $f(E, \mu_R)$ the Fermi-Dirac distribution of the left and right electrodes, respectively. μ_L and μ_R are the electrochemical potentials of the left and right electrodes, respectively. The $T_\sigma(E, V_b)$ is the transmission probability for an electron at energy E with spin σ at a bias V_b .

Acknowledgments

This work was supported by the Ministry of Science and Technology of the People's Republic of China (Grant No. 2022YFA1402901), Natural Science Foundation of China (No. 12474237,

12074301, 52371236), and Science Fund for Distinguished Young Scholars of Shaanxi Province (No. 2024JC-JCQN-09).

Conflict of interest

The authors declare no conflict of interest.

References:

- [1] X. Jiang, Q. Liu, J. Xing, N. Liu, Y. Guo, Z. Liu, and J. Zhao, *Applied Physics Reviews* **8**, 031305 (2021).
- [2] S. Xing, J. Zhou, X. Zhang, S. Elliott, and Z. Sun, *Prog. Mater. Sci.* **132**, 101036 (2023).
- [3] P. Chuang *et al.*, *Nat. Nanotechnol.* **10**, 35 (2015).
- [4] S. Datta and B. Das, *Appl. Phys. Lett.* **56**, 665 (1990).
- [5] P. J. Rajput, S. U. Bhandari, and D. Khurge, in *2024 IEEE 4th International Conference on VLSI Systems, Architecture, Technology and Applications (VLSI SATA)2024*, pp. 1.
- [6] S. A. Wolf, D. D. Awschalom, R. A. Buhrman, J. M. Daughton, S. von Molnar, M. L. Roukes, A. Y. Chtchelkanova, and D. M. Treger, *Science* **294**, 1488 (2001).
- [7] J. Gong, G. Ding, C. Xie, W. Wang, Y. Liu, G. Zhang, and X. Wang, *Advanced Science* **11**, 2307297 (2023).
- [8] E. Zhai, T. Liang, R. Liu, M. Cai, R. Li, Q. Shao, C. Su, and Y. C. Lin, *Nature Reviews Electrical Engineering* **1**, 497 (2024).
- [9] D. Zhang, A. Rahman, W. Qin, X. Li, P. Cui, Z. Zhang, and Z. Zhang, *Phys. Rev. B* **101**, 205119 (2020).
- [10] S. Zhang, R. Xu, W. Duan, and X. Zou, *Advanced Functional Materials* **29**, 1808380 (2019).
- [11] C. Lei, Y. Ma, X. Xu, T. Zhang, B. Huang, and Y. Dai, *The Journal of Physical Chemistry C* **123**, 23089 (2019).
- [12] R. J. Sun, R. Liu, J. J. Lu, X. W. Zhao, G. C. Hu, X. B. Yuan, and J. F. Ren, *Phys. Rev. B* **105**, 235416 (2022).
- [13] B. Wang, Y. Bai, C. Wang, S. Liu, S. Yao, Y. Jia, and J. Cho, *Phys. Rev. B* **110**, 094423 (2024).
- [14] X. Zhang, B. Liu, J. Huang, X. Cao, Y. Zhang, and Z.-X. Guo, *Phys. Rev. B* **109**, 205105 (2024).
- [15] L. Cao, X. Deng, G. Zhou, S.-J. Liang, C. V. Nguyen, L. K. Ang, and Y. S. Ang, *Phys. Rev. B* **105**, 165302 (2022).
- [16] Y. Chen, G. Wang, J. Guo, M. Li, H. Yuan, and H. Chen, *ACS Appl. Nano Mater.* **7**, 4302 (2024).
- [17] N. Guo, H. Lian, T. Guo, J. Lu, X. Yao, and X. Zhang, *ACS Appl. Nano Mater.* **7**, 14468 (2024).

-
- [18] Y. Wang, X. Xu, W. Ji, S. Li, Y. Li, and X. Zhao, *npj Comput. Mater.* **9**, 223 (2023).
- [19] S. Yang, Z. Zheng, H. Hao, C.-S. Liu, X. Zheng, and L. Zhang, *Phys. Rev. B* **110**, 235408 (2024).
- [20] T. Zhang, H. Guo, J. Shen, Y. Liang, H. Fan, W. Jiang, Q. Wang, and X. Tian, *npj Comput. Mater.* **10**, 238 (2024).
- [21] Y. Zhu *et al.*, *Appl. Phys. Lett.* **125**, 083504 (2024).
- [22] B. L. Chittari, Y. Park, D. Lee, M. Han, A. H. MacDonald, E. Hwang, and J. Jung, *Phys. Rev. B* **94**, 184428 (2016).
- [23] W. S. Hou, M. Q. Dong, X. Zhang, and Z.-X. Guo, *Phys. Rev. B* **110**, arXiv.2407.10438 (2024).
- [24] S. Xu, Z. Wu, Y. Dedkov, and E. Voloshina, *J. Phys. Condens. Matter.* **33**, 354001 (2021).
- [25] D. Sen and T. Saha-Dasgupta, *Phys. Rev. Mater.* **7**, 064008 (2023).
- [26] S. Kumar and U. Schwingenschlögl, *Phys. Rev. B* **94**, 035405 (2016).
- [27] Y. Lee, Y. Hwang, and Y. C. Chung, *ACS Appl. Mater. Inter.* **7**, 7163 (2015).
- [28] P. E. Blöchl, *Phys. Rev. B* **50**, 17953 (1994).
- [29] G. Kresse and J. Furthmüller, *Phys. Rev. B* **54**, 11169 (1996).
- [30] G. Kresse and J. Hafner, *Phys. Rev. B* **47**, 558 (1993).
- [31] H. J. Monkhorst and J. D. Pack, *Phys. Rev. B* **13**, 5188 (1976).
- [32] J. P. Perdew, K. Burke, and M. Ernzerhof, *Phys. Rev. Lett.* **77**, 3865 (1996).
- [33] S. L. Dudarev, G. A. Botton, S. Y. Savrasov, C. J. Humphreys, and A. P. Sutton, *Phys. Rev. B* **57**, 1505 (1998).
- [34] N. Sivadas, S. Okamoto, X. Xu, C. J. Fennie, and D. Xiao, *Nano Lett.* **18**, 7658 (2018).
- [35] S. Grimme, J. Antony, S. Ehrlich, and H. Krieg, *The Journal of Chemical Physics* **132**, 154104 (2010).
- [36] M. Brandbyge, J.-L. Mozos, P. Ordejón, J. Taylor, and K. Stokbro, *Phys. Rev. B* **65**, 165401 (2002).
- [37] S. Smidstrup *et al.*, *J. Phys. Condens. Matter.* **32**, 015901 (2019).
- [38] Z. Zhong *et al.*, *ACS Nano* **17**, 12563 (2023).
- [39] P. Singh, S. Baek, H. H. Yoo, J. Niu, J.-H. Park, and S. Lee, *ACS Nano* **16**, 5418 (2022).
- [40] M. Si, P.-Y. Liao, G. Qiu, Y. Duan, and P. D. Ye, *ACS Nano* **12**, 6700 (2018).

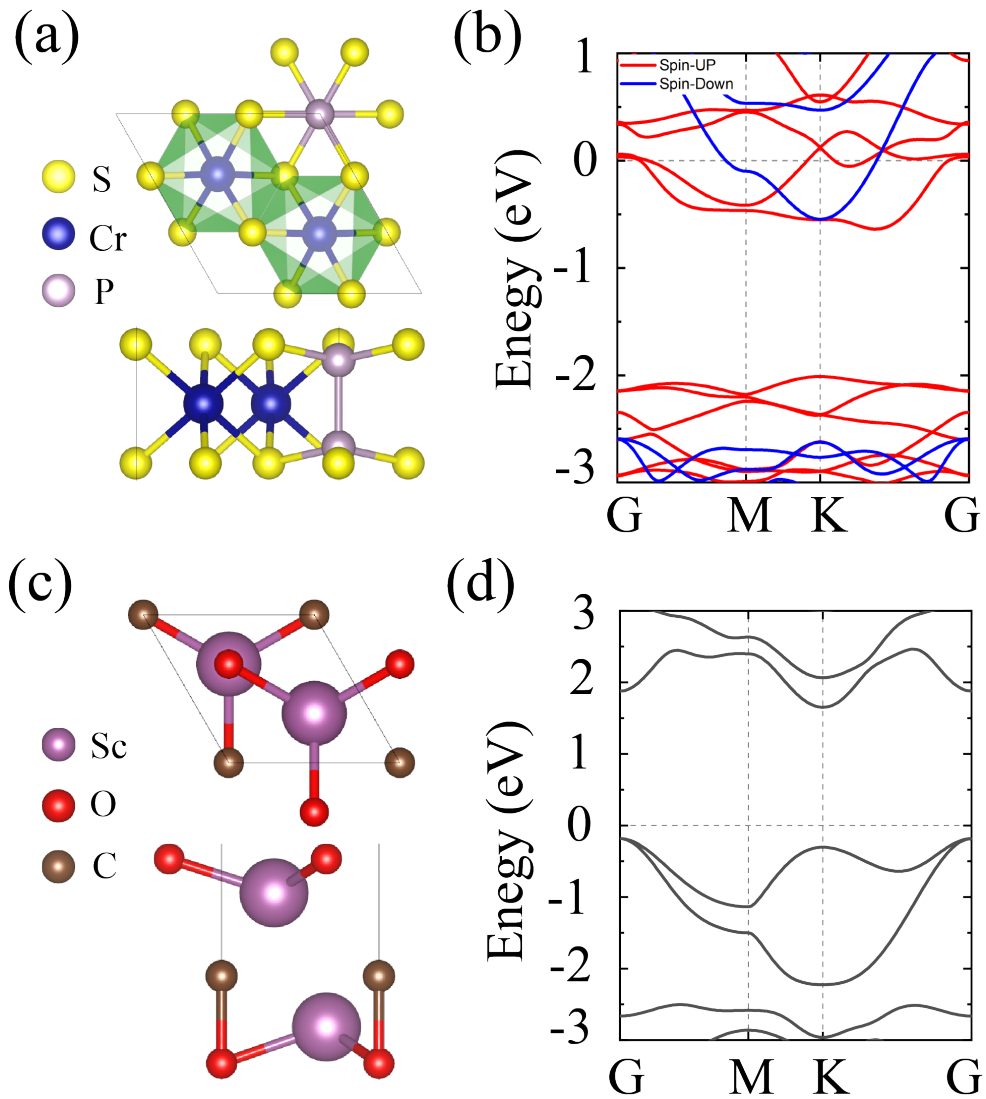


Figure 1 (a) Atomic structures of top view (top) and side view (bottom) of monolayer CrPS₃. (b) Band structure of FM of monolayer CrPS₃. (c) Atomic structures of top view (top) and side view (bottom) of monolayer Sc₂CO₂. (d) Band structure of monolayer Sc₂CO₂. The yellow, blue, light purple, great purple, red and brown represent S, Cr, P, Sc, O and C atoms, respectively.

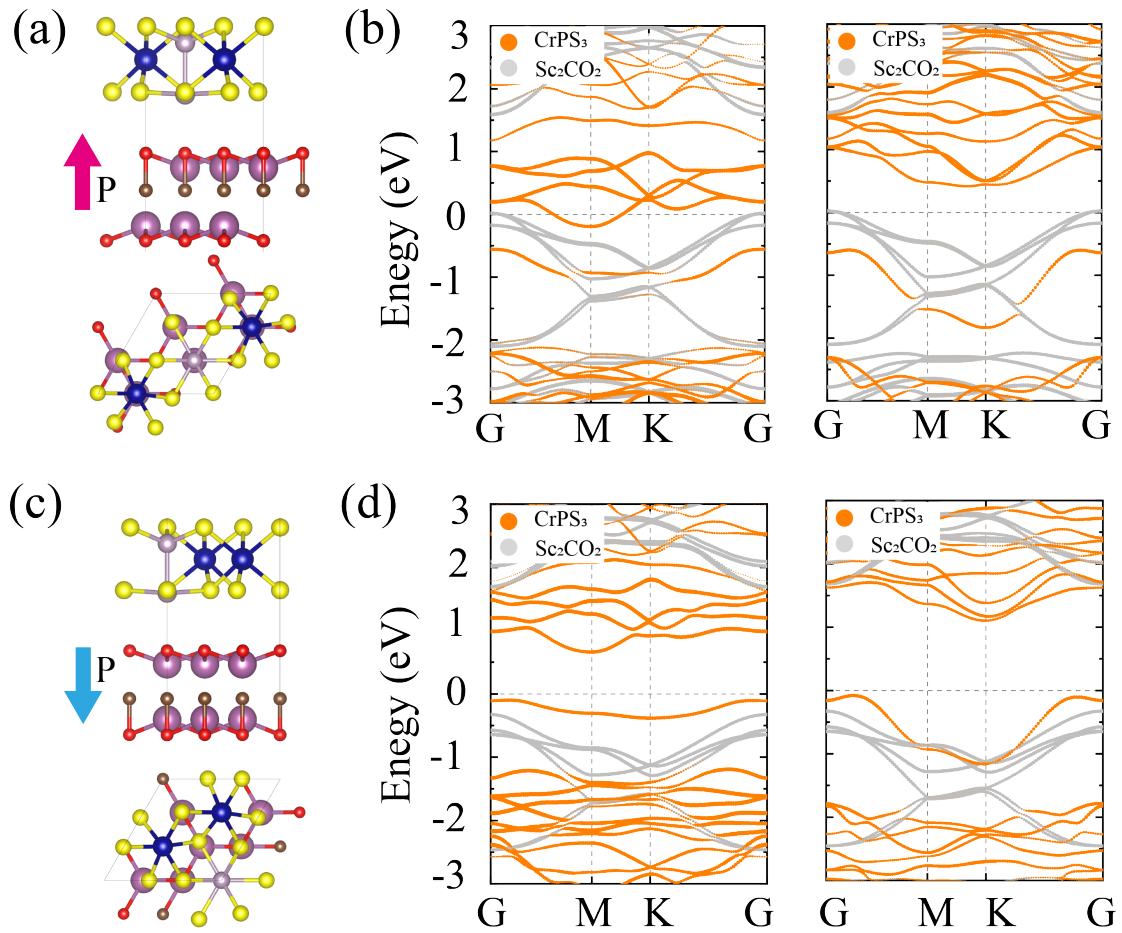


Figure 2 (a) and (c): Atomic structures of the CrPS₃/Sc₂CO₂ heterostructure with Sc₂CO₂ in (a) P ↑ and (c) P ↓ polarizations. (b) and (d): The electronic band structures of the CrPS₃/Sc₂CO₂ heterostructure with Sc₂CO₂ in (b) P ↑ and (d) P ↓ polarizations, where the left and right panels represent the spin-up and spin-down energy bands, respectively.

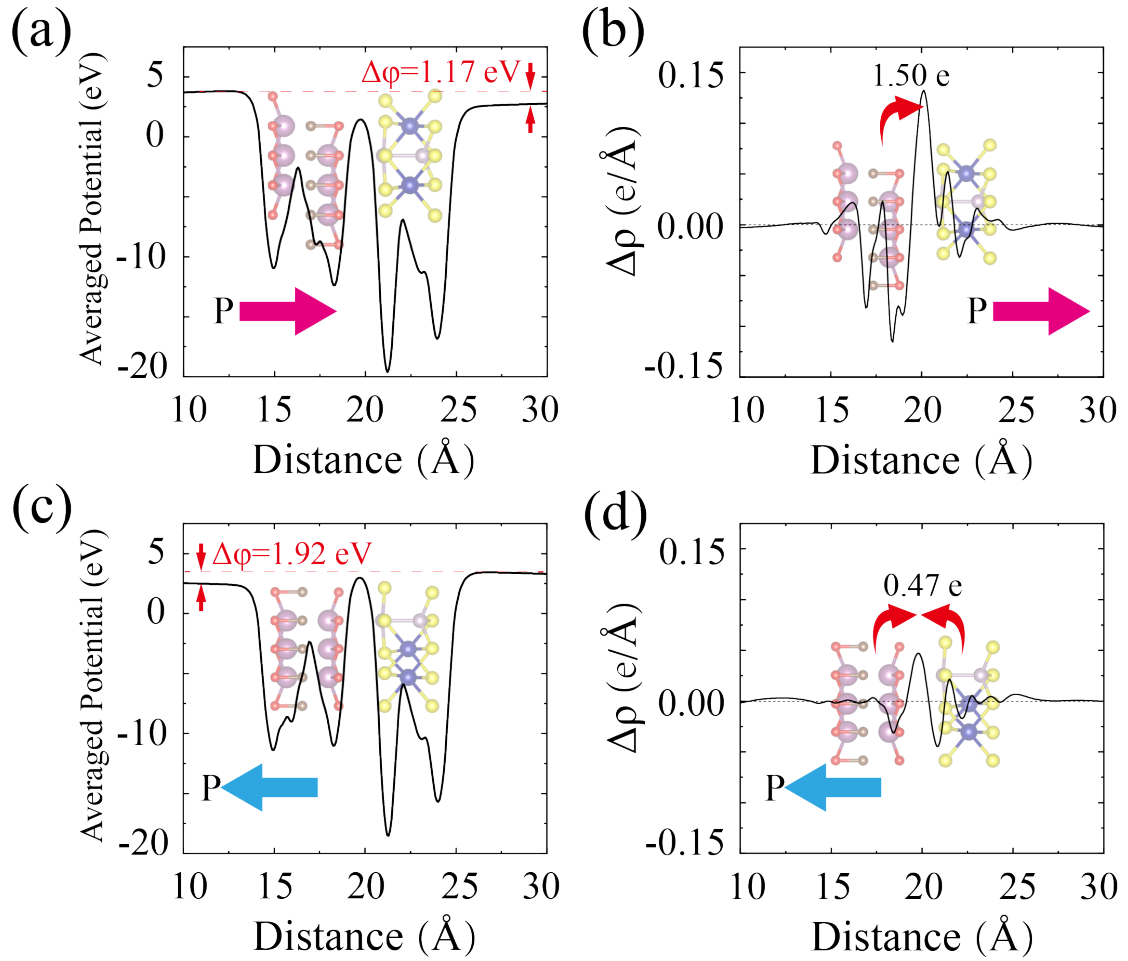


Figure 3 (a) and (c): Plane-averaged electrostatic potential of CrPS₃/Sc₂CO₂ (a) P↑ and (c) P↓ along the out-of-plane (z) direction. (b) and (d): The plane-averaged differential charge density $\Delta\rho$ of CrPS₃/Sc₂CO₂ (b) P↑ and (d) P↓ along the z direction.

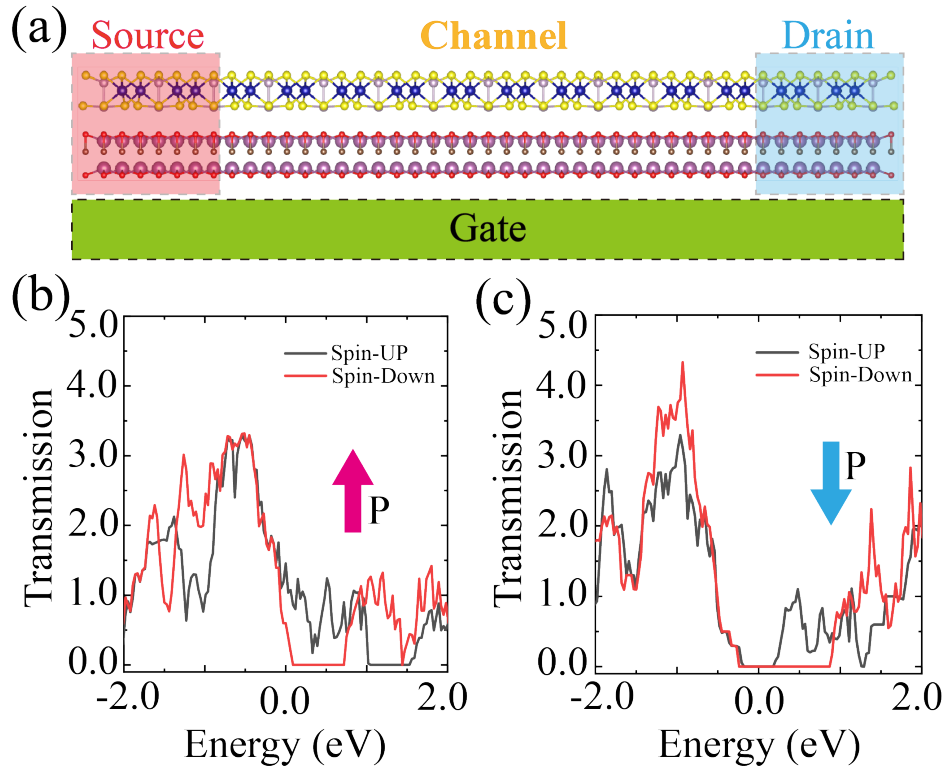


Figure 4 (a) The schematic structure of the proposed SFET based on the CrPS₃/Sc₂CO₂ heterostructure. (b) The calculated spin-polarized transmission spectrum of the SFET with Sc₂CO₂ in P↑ polarization at zero bias. (c) The calculated spin-polarized transmission spectrum of the SFET with Sc₂CO₂ in P↓ polarization at zero bias.

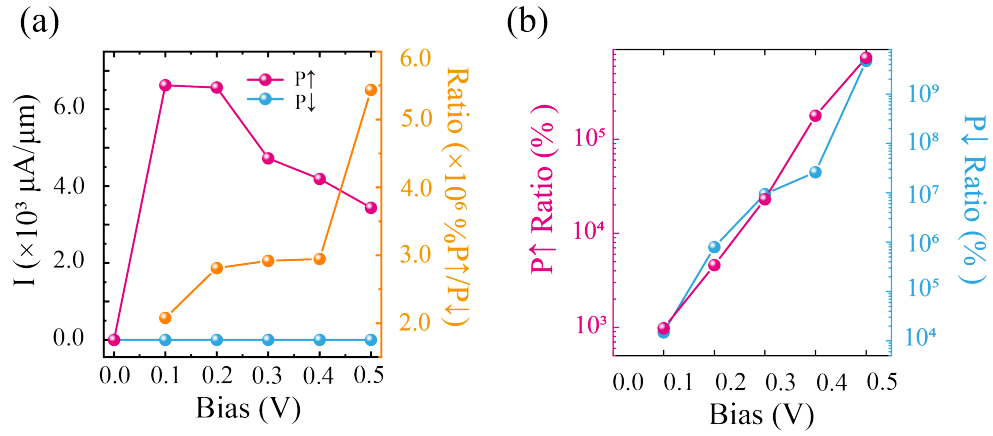


Figure 5 (a) The total current (sum of spin-up and spin-down current) with Sc₂CO₂ in P↑ (magenta line), P↓ (sky blue line) polarizations and *on/off* ratio (orange Line) under finite bias of 0.0-0.5 V. (b) The ratio of spin up and spin down current with Sc₂CO₂ in P↑ (magenta line), P↓ (sky blue line) polarizations under finite bias of 0.0-0.5 V.

Table 1 The *on/off* ratio, current of spin-up/spin-down ratio and TER of SFETs and FeFETs device.

Materials	<i>on/off</i> ratio (%)	spin-up/spin-down ratio (%)	TER (%)
CrPS ₃ /Sc ₂ CO ₂	5.4×10^6	730,000	1.6×10^{23}
FCl ₂ / Sc ₂ CO ₂ [15]	3.2×10^5	155.12	1.7×10^{17}
VSi ₂ N ₄ / Sc ₂ CO ₂ [14]	6.5×10^2	2,500	1.6×10^{10}
RuCl ₂ /Al ₂ S ₃ [16]	\	1,027	3.0×10^7
Cu/CuInP ₂ S ₆ (CIPS)/graphene [38]	10^6	\	\
In/CIPS/hBN/InSe [39]	10^6	\	\
Au/CIPS/MoS ₂ [40]	10^4	\	\